nature geoscience

ARTICLES

https://doi.org/10.1038/s41561-020-0627-9



# Slip-rate-dependent friction as a universal mechanism for slow slip events

Kyungjae Im[1,2]✉, Demian Saffer[3,4], Chris Marone[3] and Jean-Philippe Avouac[1]

**A growing body of observations worldwide has documented fault slip transients that radiate little or no seismic energy. The mechanisms that govern these slow slip events (SSEs) and their wide range of depths, slip rates, durations, stress drops and recurrence intervals remain poorly known. Here we show that slow slip can be explained by a transition from rate-weakening frictional sliding at low slip rates towards rate-neutral or rate-strengthening behaviour at higher slip rates, as has been observed experimentally. We use numerical simulations to illustrate that this rate-dependent transition quantitatively explains the experimental data for natural fault rocks representative of materials in the source regions of SSEs. With a standard constant-parameter rate-and-state friction law, SSEs arise only near the threshold for slip instability. The inclusion of velocity-dependent friction parameters substantially broadens the range of conditions for slow slip occurrence, and produces a wide range of event characteristics, which include stress drop, duration and recurrence, as observed in nature. Upscaled numerical simulations that incorporate parameters consistent with laboratory measurements can reproduce geodetic observations of repeating SSEs on tectonic faults. We conclude that slip-rate-dependent friction explains the ubiquitous occurrence of SSEs in a broad range of geological environments.**

Faults in nature can slip episodically during earthquakes, with a slip rate typically larger than 1 cm s$^{-1}$, but also in much slower transient slip events that are essentially aseismic. These include slow slip events (SSEs), which last days to weeks and are often associated with low-amplitude seismic tremors[1,2]. SSEs have been widely observed and span a range of depths along subduction plate interfaces, including Cascadia[2], Mexico[3], Japan[4], Costa Rica[5] and New Zealand[6], as well as on continental transform faults including the San Andreas[7] and North Anatolian Faults[8]. In some cases, these phenomena have been linked to elevated pore pressure based on theoretical considerations, their sensitivity to tidal stresses and their spatial correlation with zones of high P-wave to S-wave velocity ratio ($V_p/V_s$)[9–11].

SSEs result, like regular earthquakes, from unstable frictional sliding[12,13]. Previous studies showed that SSEs can arise in numerical simulations based on the rate-and-state friction[14] (RSF) formalism. Within the RSF framework, regular earthquakes (stick–slip) occur if the slipping area is larger than a critical patch size, and SSEs arise if the system is near critical. However, in this context, SSEs should be observed only over a very narrow range of parameters for which the fault lies precisely at, or very near, the stable–unstable transition[12,13] (Figs. 1 and 2). This contrasts with the ubiquitous occurrence of SSEs, which span a diversity of geological environments in nature.

Recent laboratory experiments also document a wide range of slow slip behaviours, with a gradual evolution from stable sliding to slow stick–slip and ultimately to fast slip[15–19]. This laboratory work, together with the widespread occurrence of slow slip in nature, suggests a role for processes other than those represented by the standard friction on a homogeneous fault—such as fluid-assisted dilation hardening[20], geological heterogeneities[21] or more complex frictional rheology, such as the sliding-rate dependence of RSF parameters[22–24].

In RSF theory, the critical fault weakening rate as a function of slip (characterized by the critical stiffness, $K_c \approx (a-b)\sigma'/D_c$, determines frictional stability (where $\sigma'$ is the effective normal stress, $D_c$ is the critical slip distance and $a$ and $b$ are empirical constants that define the direct and evolution effects, respectively) (Methods)[25]. In the standard form of RSF, the rate parameter $(a-b)$ and $D_c$ are constant and independent of the sliding velocity. However, recent laboratory measurements on both natural and synthetic fault gouges, which include drill core from faults that are known to host SSEs, indicate that these parameters actually vary systematically with slip velocity[26–28]. The velocity dependence of $D_c$ and $(a-b)$ was reported more than a decade ago for some materials[29,30], and was speculated as a potential explanation for episodic slow slip[22–24]. These results suggest qualitatively that the increased stability at a high slip velocity suppresses the acceleration of slip, and accordingly widens the range of conditions for a slow earthquake generation. Numerical simulations in one dimension and in two dimensions successfully produced slow slip evolution and propagation by incorporating velocity-dependent stability criteria[22,24]. Here we investigate this hypothesis further by taking advantage of newly available laboratory data from natural fault zones that host slow earthquakes and compare the observations of SSEs with numerical simulations. The dynamic simulations were used to first reproduce the behaviour observed in the laboratory[16] and second to upscale to in situ fault-zone conditions.

## Numerical simulations of laboratory observations

Our simulations for both constant (Fig. 1a) and velocity-dependent (Fig. 1b) RSF parameters are consistent with the theoretically defined stability criterion[25] ($\kappa = K/K_c = 1$, where $K$ is the system stiffness; black lines in Fig. 1a,b). Note that $K_c$ must be evaluated in a general form (Methods and Rice and Ruina[25]) to account for rate-dependent

[1]Geology and Planetary Science Division, California Institute of Technology, Pasadena, CA, USA. [2]Department of Energy and Mineral Engineering, EMS Energy Institute and G3 Center, The Pennsylvania State University, University Park, PA, USA. [3]Department of Geosciences, EMS Energy Institute, and G3 Center, The Pennsylvania State University, University Park, PA, USA. [4]University of Texas Institute for Geophysics and Dept. of Geological Sciences, University of Texas, Austin, TX, USA. ✉e-mail: kjim@caltech.edu

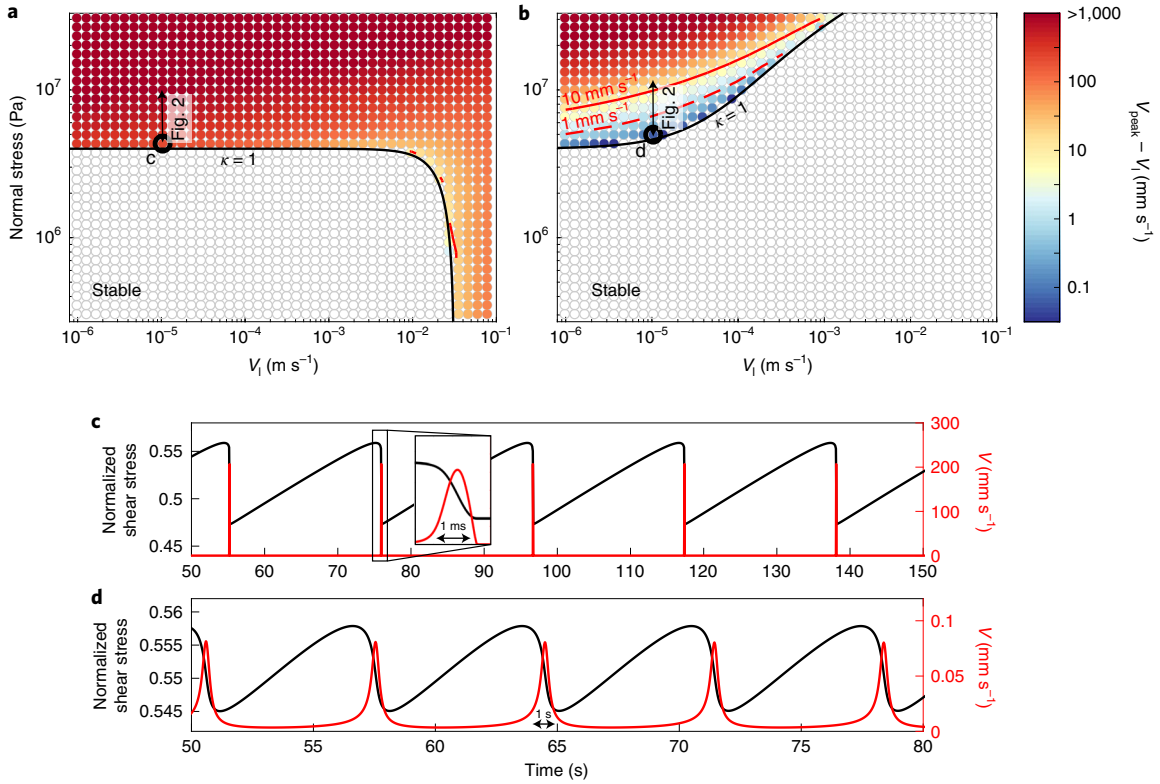


**Fig. 1 | Conditions for episodic slow slip. a**,**b**, Evolution of the modelled peak slip velocity for constant RSF parameters (**a**) and velocity-dependent $D_c$ and $a$ (**b**). See Extended Data Fig. 1 for cases that show the separate effects of the velocity dependence of $D_c$ and $a$. Filled circles represent unstable periodic oscillations (as in **c**,**d**). Empty circles denote stable sliding. The black line indicates the analytically calculated stability criterion ($\kappa = 1$) (ref. [25]). Black circles denote the cases presented in **c**,**d** and arrows denote the normal stress range in Fig. 2. **c**,**d**, Limit cycle oscillation of the normalized shear stress (black), $K(\delta_{lp} - \delta)/\sigma'$ (see equation (3) in Methods), and velocity (red) for the closest case to $\kappa = 1$ at a loading velocity ($V_l$) of $10^{-5}$ m s$^{-1}$ (see Methods for details).

RSF parameters. All cases with $\kappa < 1$ converged towards a repeating unstable slip (filled circles), whereas all cases with $\kappa > 1$ converged to stable sliding (empty circles) (Fig. 1a,b). In both cases, and as predicted by theory, slip transitioned from stable to unstable as the normal stress is increased. In the experimental data[16], the transition occurred at higher normal stress when the loading rate was increased; that is, the slip stabilized at a higher velocity (Extended Data Fig. 2a). This is not expected for constant-parameter (regular) RSF, because the critical stiffness $K_c$ is only expected to increase with slip velocity (equation (6), Methods). The observations are, however, consistent with a rate dependence of $D_c$ and $(a-b)$, and this behaviour was reproduced by simulations that account for this effect (Extended Data Fig. 2).

Another important difference is that constant RSF parameters predicted an abrupt transition from steady sliding to fast earthquake-like stick–slip events, whereas rate-dependent RSF parameters predicted a more gradual transition (blue regions in Fig. 1b) and a broader range of loading velocities and normal stresses that yield a spectrum of SSEs, consistent with field and laboratory results[15–19]. This difference is also evident from the comparison of time series of both normalized shear stresses and the velocity of unstable sliding closest to the stability boundary ($\kappa = 1$) (Fig. 1c,d). Constant-parameter simulations for the laboratory experimental conditions produced regular stick–slip with a peak velocity ($V_{peak}$) of 20 cm s$^{-1}$ and slip duration of ~1 ms (Fig. 1c). In contrast, the cases with velocity-dependent parameter resulted in slow events with a $V_{peak}$ of ~80 μm s$^{-1}$ and slip duration of ~1 s (Fig. 1d).

The expansion of the slow earthquake domain is particularly evident when simulations for a given loading rate are compared with laboratory experiments as a function of $\kappa$ (Fig. 2). Simulations with velocity-dependent RSF parameters agree much better with the laboratory results. The constant-parameter case exhibited an abrupt transition at $\kappa = 1$ (the stability threshold), which resulted in about 2–3 orders of magnitude larger peak velocities (Fig. 2a) and about 3–5 times larger stress drops (Fig. 2b) than the laboratory observations. In contrast, cases with velocity-dependent RSF parameters produce a gradual evolution of slip behaviour as $\kappa$ approaches unity, in a substantially better agreement with the laboratory experimental data. We note that the fit to laboratory data is not perfect; for $V_{peak} > 1$ mm s$^{-1}$, the laboratory measurements of $V_{peak}$ are slower than the model predictions (Fig. 2a). The overprediction of $V_{peak}$ may be explained by a finite sampling frequency, derivation of velocity from discrete measurements in the laboratory or other factors unaccounted for in our analysis.

Our results also demonstrate that the peak slip velocity in slow stick–slip events remains consistently lower than a commonly reported 'cutoff velocity' ($V_a$) that has been inferred at the transition from a negative ($a-b<0$) to a positive ($a-b>0$) rate dependence of friction; furthermore, such a transition is not necessarily required to produce a spectrum of slow stick–slip. This arises because slip behaviour exhibits a strong dependence on the rate of friction change with velocity (second term in equation (10), Methods) as well as the absolute value of rate dependence.

## Upscaled simulations and application to subduction zones

With a spring-slider approximation approach, we conducted multiple simulations with parameters representative of a generic subduction zone (Fig. 3a,b), modified from the parameters of

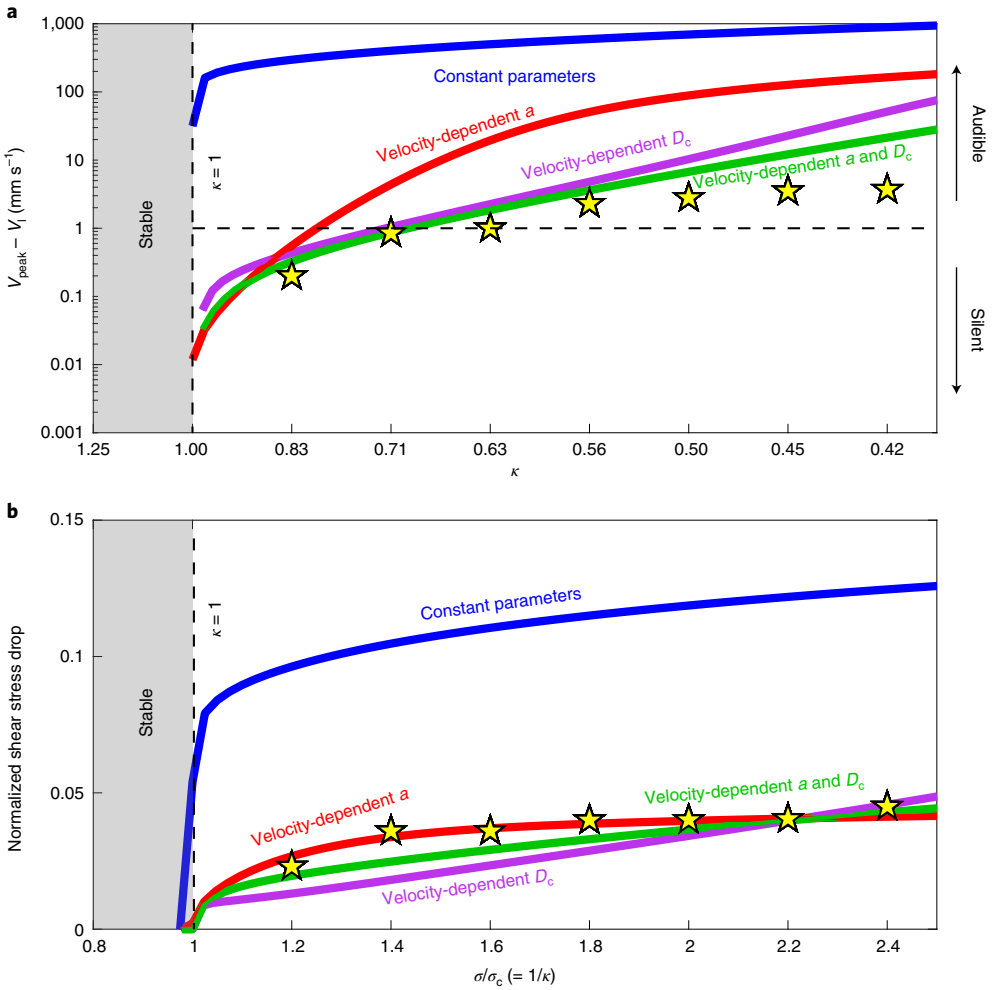


**Fig. 2 | $V_{peak}$ and normalized stress drop as a function of κ. a**,**b**, $V_{peak}$ (**a**) and normalized stress drop (**b**) as a function of κ. The loading velocity is 10 μm s$^{-1}$. For constants and velocity-dependent *a* and $D_c$ we use the same parameters as in Fig. 1 (see Methods for the detailed input parameters). The *x* axis in **b** shows the normal stress ($\sigma$) normalized by the normal stress at the stability transition ($\sigma_c$); the *x* axis in **a** shows the corresponding values of κ. Yellow stars denote experimental results[16]. Models with rate-dependent RSF parameters predict a slow stick–slip ($V$<1mms$^{-1}$) for values of κ as low as ~0.7.

Scholz[31] for regular (constant parameter) RSF. At a low slip rate ($V \ll V_a = 10^{-9}$ m s$^{-1}$), steady-state friction was assumed to be rate weakening ($a_0 - b < 0$) for depths between 7.5 and 37.5 km, and rate strengthening ($a_0 - b > 0$) above and below this. The value of $a_0 - b$ was set constant at −0.003 between 15 and 30 km, and varied linearly with depth elsewhere (Fig. 3b). We considered two scenarios, one in which pore pressure is 70% of the lithostatic pressure, presumably representative of the typical pore pressure along subduction megathrusts[32], and a second case in which the pore pressure is set to 95% of the lithostatic pressure, which falls in the range of pore pressures that approach lithostatic values, as suggested on the basis of forearc wedge taper angles and geophysical survey data[10,32]. We then considered the additional effect of the velocity dependence of $(a - b)$ and $D_c$, and explored a parameter space consistent with recently reported laboratory data for real fault rocks[27,30].

With regular RSF, the entire rate-weakening domain between depths of 7.5 and 37.5 km produced simulated stick–slip events with a high $V_{peak}$ (>1 cm s$^{-1}$) and relatively large stress drops (>1 MPa), even if a high pore pressure was assumed (Fig. 3c,d). To generate slow stick–slip events for a case in which the RSF parameters are constant, the effective normal stress must remain very small, and a near-neutral RSF behaviour (with $b - a \ll 10^{-4}$) required. This condition is met only in a very narrow zone at the transition from the rate-strengthening to the rate-weakening behaviour that is not resolved with our simulations. This result is consistent with previously reported fault-plane simulation results, which show that the range of fault length (stiffness) that hosts the slow slip is too small to be explained by the standard constant parameter RSF[13].

However, with velocity-dependent RSF parameters, slow slip transients (with velocities similar to those in subduction zone SSEs, 1 nm s$^{-1}$ to 1 μm s$^{-1}$) were simulated over a considerably broader region that spanned this transition zone, and with a wider range of event characteristics (Fig. 3). Notably, all of our simulation results with velocity-dependent $(a - b)$ and $D_c$ yield $V_{peak} < 1$ mm s$^{-1}$, which we regard as 'slow' relative to the centimetres or metres per second slip velocities typical of ordinary earthquakes (Fig. 3c, red and blue curves). Although not required, a higher pore pressure (lower effective normal stress) led to a decreased peak slip velocity, and hence further broadened the region in which slow slip occurred. Stress drop and recurrence interval were also sensitive to pore pressure (Fig. 3d,e), such that modest variations were able to produce simulated SSEs that span a wide spectrum of rates, recurrence and

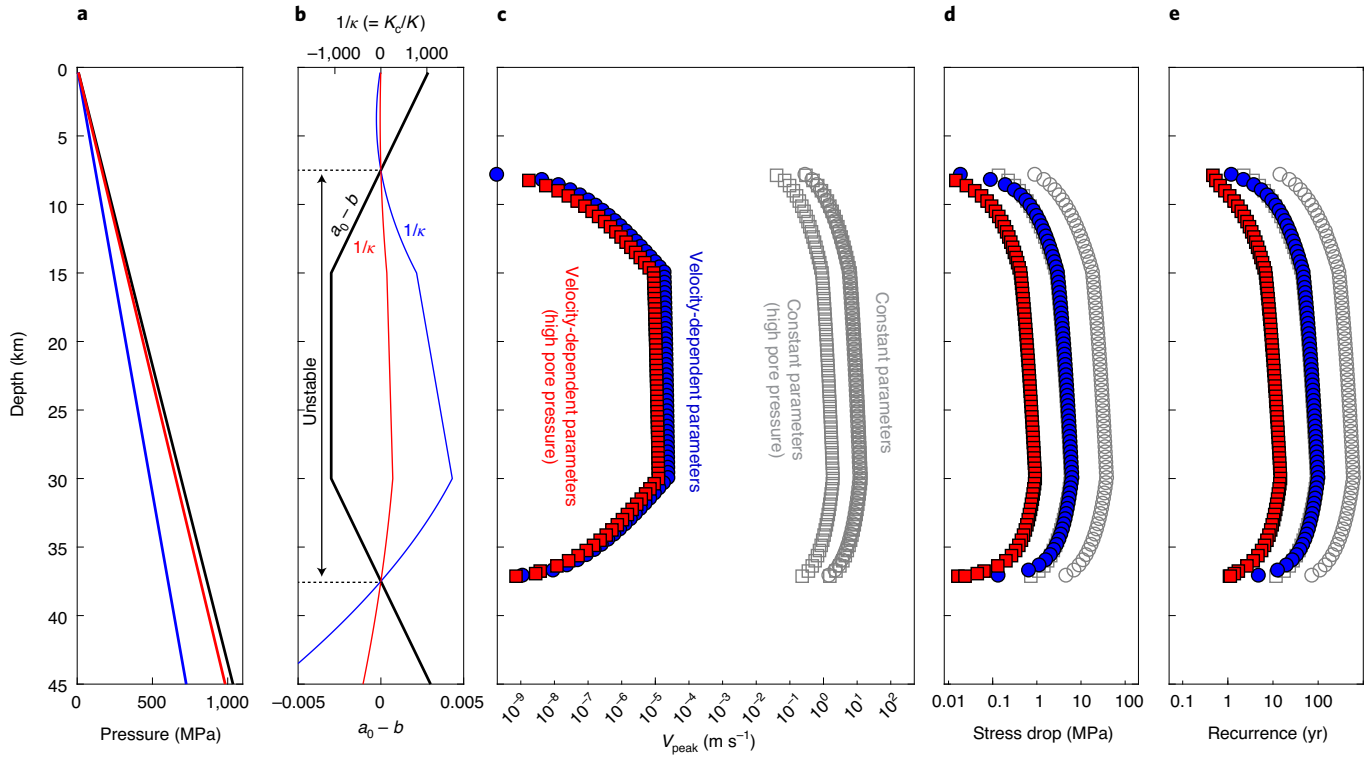


**Fig. 3 | Characteristics of stick-slip events as a function of depth for a generic subduction megathrust.** Each circle in **c**, **d** and **e** represents single-degree-of-freedom simulation results using normal stress and $a_0 - b$ shown in **a** and **b**. **a**, Pore pressures at 70% (blue line) and 95% (red line) of the lithostatic stress (black line). **b**, Simulation input $a_0 - b$ (black), and stability criterion shown as $1/\kappa$ (line colours correspond to the pore pressure in **a**). **c**–**e**, Simulated peak slip velocity (**c**), stress drop (**d**) and recurrence (**e**) for velocity-dependent parameters (coloured symbols) and constant parameters (regular RSF, grey symbols). See Methods for detailed velocity dependence of $a$ and $D_c$.

durations, consistent with the broad range of observed SSE behaviour in nature.

## Comparison to natural SSEs

We considered case examples of well-characterized repeating SSEs in Cascadia (United States)[33], Hikurangi[6] (New Zealand), Ryukyu[34] (Japan) and the Guerrero gap[35] (Mexico) (Fig. 4). These examples span a wide range of depths, from near surface to ~40 km, and a range of recurrence intervals from subannual to decadal. We explored a parameter space consistent with the laboratory constraints[16,27,29] (Extended Data Fig. 3b). Assuming that the global positioning system (GPS) displacement is proportional to the fault slip, we successfully reproduced the evolution and behaviour of these well-characterized SSEs with only a modest adjustment of the model parameters within the range of experimental data, using a single-degree-of-freedom approximation. Given that this approximation is not strictly valid, as it is clear that SSE can expand and propagate[33], we carried out tests (Extended Data Fig. 5) and the results indicated that this is still a reasonable first-order approximation for typical rates of propagation of SSEs.

Interestingly, our simulations also capture the asymmetric fast-acceleration and slow-deceleration characteristics of SSEs, which are most prominent in the Ryukyu and, to a lesser degree, the Mexican examples, and which can be observed in most of the GPS stations regardless of their relative locations to the slipping patch[36,37]. This behaviour emerges in our simulations as a result of the fundamental characteristics of RSF that lead to a fast acceleration at $(a-b)<0$ (nucleation phase in the simulation) and a slow deceleration for $(a-b)\approx 0$ or $(a-b)>0$ (when slip decelerates). However, we acknowledge that other factors, which include three-dimensional effects that are ignored in our simulations, could also help explain the asymmetric slip–velocity pulse of SSEs in nature.

We do not claim that the model parameters used in each of these simulations are uniquely constrained. However, we emphasize that a framework with rate-dependent $(a-b)$ and $D_c$, which is consistent with recent laboratory measurements for materials from natural tectonic faults that host SSEs, together with a low effective normal stress, can produce a broad range of episodic SSEs with characteristics comparable to those of observed SSEs.

Our work quantitatively illuminates one potential underlying mechanism to explain the widespread occurrence and broad spectrum of SSE slip rates. We found that recurrent slow slip can occur over a much wider range of conditions if the RSF formalism is adjusted so that frictional sliding transitions from rate weakening at a low slip rate to a lesser rate-weakening or rate-neutral behaviour at a higher slip rate, as is observed in laboratory experiments on samples representative of lithologies that host SSEs in nature[27,28]. Our results provide a resolution to the apparent paradox that SSEs are widespread globally and occur over a broad range of depths and geological environments and span a spectrum of slip rates and durations, yet the predictions of regular RSF laws restrict their occurrence to a very narrow set of conditions.

## Online content

Any methods, additional references, Nature Research reporting summaries, source data, extended data, supplementary information, acknowledgements, peer review information; details of author contributions and competing interests; and statements of

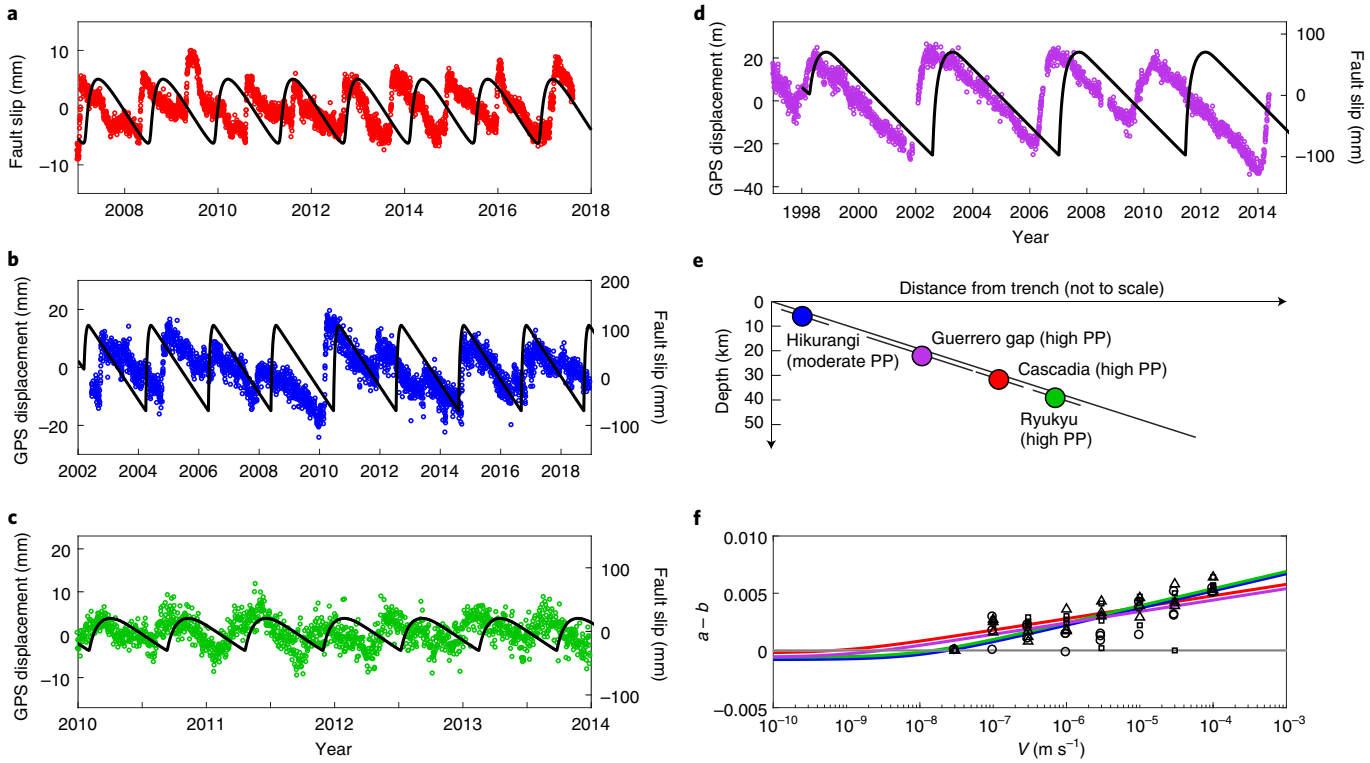


**Fig. 4 | Comparison with observed SSEs. a–d**, Estimated slow slip history (coloured dots) and simulations (black lines) for examples of repeating SSEs observed at Cascadia North[33] (inverted from GPS data) (**a**), Hikurangi (station GISB)[6] (**b**), Ryuku (station J750)[34] (**c**) and Mexican megathrusts (station CAYA)[35] (**d**). **e**, Schematic section of the subduction megathrusts showing the estimated depths of SSE for the case examples and equivalent fault length used in the simulations ($L = 50$ km for the Guerrero gap on the Mexican megathrust, $L = 20$ km for the others). Pore pressure (PP) was set to 97.5, 70, 95 and 95% of the lithostatic pressure for the Cascadia, Hikurangi, Ryukyu and Guerrero gap simulations, respectively. **f**, The velocity dependence of $(a - b)$ for each simulation is colour-coded as in the other panels and the symbols show experimental data for $(a - b)$ (ref. [27]) (Extended Data Fig. 3).

data and code availability are available at https://doi.org/10.1038/s41561-020-0627-9.

Received: 23 December 2019; Accepted: 28 July 2020;
Published online: 7 September 2020

## References

1. Obara, K., Hirose, H., Yamamizu, F. & Yamamizu, K. Episodic slow slip events accompanied by non-volcanic tremors in southwest Japan subduction zone. *Geophys. Res. Lett.* **31**, L23602 (2004).
2. Dragert, H., Wang, K. & James, S. T. A silent slip event on the deeper Cascadia subduction interface. *Science* **292**, 1525–1528 (2001).
3. Kostoglodov, V. et al. A large silent earthquake in the Guerrero seismic gap, Mexico. *Geophys. Res. Lett.* **30**, 1807 (2003).
4. Kano, M. et al. Development of a slow earthquake database. *Seismol. Res. Lett.* **89**, 1566–1575 (2018).
5. Jiang, Y. et al. Slow slip events in Costa Rica detected by continuous GPS observations, 2002–2011. *Geochem. Geophys. Geosyst.* **13** https://doi.org/10.1029/2012gc004058 (2012).
6. Wallace, L. M. et al. Slow slip near the trench at the Hikurangi subduction zone, New Zealand. *Science* **352**, 701–704 (2016).
7. Tymofyeyeva, E. et al. Slow slip event on the southern San Andreas fault triggered by the 2017 $M_w$8.2 Chiapas (Mexico) earthquake. *J. Geophys. Res Solid Earth* **124**, 9956–9975 (2019).
8. Rousset, B. et al. An aseismic slip transient on the North Anatolian Fault. *Geophys. Res. Lett.* **43**, 3254–3262 (2016).
9. Hawthorne, J. C. & Rubin, A. M. Tidal modulation of slow slip in Cascadia. *J. Geophys. Res. Solid Earth* **115**, https://doi.org/10.1029/2010jb007502 (2010).
10. Kodaira, S. et al. High pore fluid pressure may cause silent slip in the Nankai Trough. *Science* **304**, 1295–1298 (2004).
11. Gao, X. & Wang, K. L. Rheological separation of the megathrust seismogenic zone and episodic tremor and slip. *Nature* **543**, 416–419 (2017).
12. Liu, Y. J. & Rice, J.R. Aseismic slip transients emerge spontaneously in three-dimensional rate and state modeling of subduction earthquake sequences. *J. Geophys. Res.* **110** https://doi.org/10.1029/2004JB003424 (2005).
13. Rubin, A. M. Episodic slow slip events and rate-and-state friction. *J. Geophys. Res. Solid Earth* **113**, B11414 (2008).
14. Marone, C. Laboratory-derived friction laws and their application to seismic faulting. *Annu. Rev. Earth Planet. Sci.* **26**, 643–696 (1998).
15. Scuderi, M. M., Collettini, C., Viti, C., Tinti, E. & Marone, C. Evolution of shear fabric in granular fault gouge from stable sliding to stick slip and implications for fault slip mode. *Geology* **45**, 731–734 (2017).
16. Leeman, J. R., Marone, C. & Saffer, D. M. Frictional mechanics of slow earthquakes. *J. Geophys. Res. Solid Earth* **123**, 7931–7949 (2018).
17. Leeman, J. R., Saffer, D. M., Scuderi, M. M. & Marone, C. Laboratory observations of slow earthquakes and the spectrum of tectonic fault slip modes. *Nat. Commun.* **7** https://doi.org/10.1038/ncomms11104 (2016).
18. Baumberger, T., Heslot, F. & Perrin, B. Crossover from creep to inertial motion in friction dynamics. *Nature* **367**, 544–546 (1994).
19. Mitchell, E. K., Fialko, Y. & Brown, K. M. Frictional properties of gabbro at conditions corresponding to slow slip events in subduction zones. *Geochem. Geophys. Geosystems* **16**, 4006–4020 (2015).
20. Segall, P., Rubin, A. M., Bradley, A. M. & Rice, J. R. Dilatant strengthening as a mechanism for slow slip events. *J. Geophys. Res. Solid Earth* **115** https://doi.org/10.1029/2010jb007449 (2010).
21. Skarbek, R. M., Rempel, A. W. & Schmidt, D. A. Geologic heterogeneity can produce aseismic slip transients. *Geophys. Res. Lett.* **39** https://doi.org/10.1029/2012gl053762 (2012).
22. Shibazaki, B. & Shimamoto, T. Modelling of short-interval silent slip events in deeper subduction interfaces considering the frictional properties at the unstable-stable transition regime. *Geophys. J. Int.* **171**, 191–205 (2007).
23. Kaproth, B. M. & Marone, C. Slow earthquakes, preseismic velocity changes, and the origin of slow frictional stick-slip. *Science* **341**, 1229–1232 (2013).
24. Rubin, A. M. Designer friction laws for bimodal slow slip propagation speeds. Geochem. *Geophys. Geosyst.* **12** https://doi.org/10.1029/2010GC003386 (2011).
25. Rice, J. R. & Ruina, A. L. Stability of steady frictional slipping. *J. Appl. Mech. Trans. ASME* **50**, 343–349 (1983).

26. Ikari, M. J., Saffer, D. M. & Marone, C. Frictional and hydrologic properties of clay-rich fault gouge. *J. Geophys. Res. Solid Earth* **114** https://doi.org/10.1029/2008jb006089 (2009).
27. Ikari, M. J. & Saffer, D. M. Comparison of frictional strength and velocity dependence between fault zones in the Nankai accretionary complex. *Geochem. Geophys. Geosyst.* **12** https://doi.org/10.1029/2010gc003442 (2011).
28. Rabinowitz, H. S. et al. Frictional behavior of input sediments to the Hikurangi trench, New Zealand. *Geochem. Geophys. Geosyst.* **19**, 2973–2990 (2018).
29. Mair, K. & Marone, C. Friction of simulated fault gouge for a wide range of velocities and normal stresses. *J. Geophys. Res. Solid Earth* **104**, 28899–28914 (1999).
30. Saffer, D. M. & Marone, C. Comparison of smectite- and illite-rich gouge frictional properties: application to the updip limit of the seismogenic zone along subduction megathrusts. *Earth Planet. Sci. Lett.* **215**, 219–235 (2003).
31. Scholz, C. H. Earthquakes and friction laws. *Nature* **391**, 37–42 (1998).
32. Saffer, D. M. & Tobin, H. J. Hydrogeology and mechanics of subduction zone forearcs: fluid flow and pore pressure. *Annu. Rev. Earth Planet. Sci.* **39**, 157–186 (2011).
33. Michel, S., Gualandi, A. & Avouac, J.-P. Similar scaling laws for earthquakes and Cascadia slow-slip events. *Nature* **574**, 522–526 (2019).
34. Kano, M., Fukuda, J., Miyazaki, S. & Nakamura, M. Spatiotemporal evolution of recurrent slow slip events along the southern Ryukyu subduction Zone, Japan, from 2010 to 2013. *J. Geophys. Res. Solid Earth* **123**, 7090–7107 (2018).
35. Gualandi, A., Perfettini, H., Radiguet, M., Cotte, N. & Kostoglodov, V. GPS deformation related to the $M_w$ 7.3, 2014, Papanoa earthquake (Mexico) reveals the aseismic behavior of the Guerrero seismic gap. *Geophys. Res. Lett.* **44**, 6039–6047 (2017).
36. Radiguet, M. et al. Slow slip events and strain accumulation in the Guerrero gap, Mexico. *J. Geophys. Res. Solid Earth* **117** https://doi.org/10.1029/2011JB008801 (2012).
37. Heki, K. & Kataoka, T. On the biannually repeating slow-slip events at the Ryukyu Trench, southwestern Japan. *J. Geophys. Res. Solid Earth* **113** https://doi.org/10.1029/2008JB005739 (2008).

## Methods

**Stability analysis with velocity-dependent RSF parameters.** In the RSF framework, friction is dependent on the slip velocity ($V$) and a state variable ($\theta$) (ref. [14]). The most widely used form is:

$$\mu = \mu_0 + a\ln\left(\frac{V}{V_0}\right) + b\ln\left(\frac{V_0\theta}{D_c}\right) \quad (1)$$

where $\mu_0$ is a reference friction coefficient at reference velocity $V_0$. Negative values of the quantity $(a-b)$ represent a velocity-weakening behaviour, such that friction decreases with increased slip rate, which is a prerequisite for unstable slip[25,38]. Positive values of $(a-b)$ indicate a velocity-strengthening behaviour, which is inherently stable.

Several formulations define the evolution of the frictional state $\theta$. In this work, we used the Ruina (slip) law, which provides the best match to laboratory observations[39,40]:

$$\frac{d\theta}{dt} = -\frac{V\theta}{D_c}\ln\left(\frac{V\theta}{D_c}\right) \quad (2)$$

Considering a one degree of freedom spring-slider system with elastic interaction, the force balance that governs the motion can be written in dimensionless form as:

$$\frac{M\ddot{\delta}}{\sigma'} = \frac{K(\delta_{lp}-\delta)}{\sigma'} - \mu \quad (3)$$

where $\delta_{lp}$ is load point displacement, $\delta$ is slider displacement, $M$ is mass per unit area (kg m$^{-2}$) and $K$ is stiffness expressed in units of shear stress per unit slip (Pa m$^{-1}$). Equation (3) shows that the normalized shear stress $K(\delta_{lp}-\delta)/\sigma'$ and friction $\mu$ decouple when the motion is dominated by inertia ($M\ddot{\delta}/\sigma'$). In this work, we used the normalized shear stress to define the magnitudes of stick–slip stress drop. In the stick-slip cycle, this normalized stress drop is almost identical to the friction drop unless inertia is substantial[41].

The criterion for unstable sliding depends on the ratio between $K$ and the critical weakening rate (stiffness) of the fault zone ($K_c$):

$$\kappa = \frac{K}{K_c} \quad (4)$$

Sliding is unstable for $\kappa<1$ and stable for $\kappa>1$. For $\kappa<1$, fault weakening outpaces the reduction in stress due to elastic unloading during slip, which results in a force imbalance and runaway instability[31].

The critical stiffness $K_c$ for a more generalized case with velocity-dependent friction is[25]:

$$K_c = -\frac{\sigma' V[d\mu_{ss}(V)/dV]}{D_c}\left\{1+\frac{MV}{\sigma' D_c[\partial\mu(V,\theta)/\partial V]}\right\} \quad (5)$$

where $\mu_{ss}(V)$ is the steady state friction at velocity $V$. Given equations (1) and (2), the parameter $\mu_{ss}(V)$ can be written as $\mu_{ss}=\mu_0+(a-b)\ln(V/V_0)$. For one state variable and regular RSF (constant $a$, $b$ and $D_c$), equation (5) simplifies to:

$$K_c = \frac{(b-a)\sigma'}{D_c}\left(1+\frac{MV^2}{\sigma' aD_c}\right) \quad (6)$$

The second bracketed term in equations (5) and (6) is a dimensionless inertial 'dynamic' parameter[41]. The influence of this term can be observed in Fig. 1a as a velocity-driven stability transition at $V_1>1$ cm s$^{-1}$. In the other simulations, this term is not important due to the low loading rates and/or velocity dependence of the $a$ parameter. However, this only means that the inertial influence is negligible in controlling stability transitions; mass (that is, inertia) is essential to define slip motions (such as $V_{peak}$, recurrence and friction drop), except for cases with extremely small accelerations (for example, the slow slip examples in Fig. 4).

**Stiffness and mass.** For upscaled simulations of SSEs, we used a lumped stiffness and mass approximation. The stiffness $K$ of the spring-slider system that represents the dynamics of slip on a fault of characteristic length $L$ embedded in an elastic medium is[42]:

$$K = \frac{G}{(1-\nu)L} \quad (7)$$

where $G$ is the shear modulus and $\nu$ is Poisson's ratio. In all the simulations, we used $K=4$ MPa m$^{-1}$. Assuming $\nu=0.25$, this lumped stiffness is equivalent to a fault patch 10 km length within a crust with a shear modulus of 30 GPa.

We used $M=600{,}000$ kg m$^{-2}$, which is equivalent to a rock mass at ~222 m depth (density 2,700 kg m$^{-3}$). Note that the influence of the mass in all of our upscaled slow slip simulations (velocity-dependent parameter cases in Fig. 3 and all simulations in Fig. 4) is negligible, as the acceleration is low. To verify the negligible influence of mass for constant parameter cases, we conducted a set of simulations with two orders of magnitude variation in mass (60,000, 600,000 and 6,000,000 kg m$^{-2}$; Extended Data Fig. 4). The calculations show that this choice has little effect on the results; even for the largest mass there is an abrupt $V_{peak}$ jump at the transition.

**Velocity dependence.** We conducted our simulations with both constant and velocity-dependent friction parameters. On the basis of previous laboratory observations (Extended Data Fig. 3)[26–28,43–45], we defined a log-linear dependence on velocity for the RSF parameters $a$ and $D_c$:

$$a(V) = a_0 + S_a\log_{10}\frac{V_a+V}{V_a} \quad (8)$$

$$D_c(V) = D_{c0} + S_{D_c}\log_{10}\frac{V_{D_c}+V}{V_{D_c}} \quad (9)$$

In equations (8) and (9), both parameters are roughly constant for $V<V_a$ and $V<V_{D_c}$ at the values $a=a_0$ and $D_c=D_{c0}$, and both increase log linearly for $V>V_a$ and $V>V_{D_c}$, with slopes of $S_a$ and $S_{D_c}$ per decade in velocity.

With velocity dependent parameters, an analytical expression that defines the stability transition can be obtained following from Rice and Ruina[25]. The expanded expressions are:

$$\frac{d\mu_{ss}}{dV} = \frac{a-b}{V} + \frac{S_a\log_{10}e}{V+V_a}\ln\frac{V}{V_0} \quad (10)$$

and

$$\frac{\partial\mu}{\partial V} = \frac{a}{V} + \frac{S_a\log_{10}e}{V+V_a}\ln\frac{V}{V_0} - \frac{S_{D_c}\log_{10}e}{V+V_{D_c}}\frac{b}{D_c} \quad (11)$$

The critical stiffness $K_c$ can be expressed by substituting equations (10) and (11) into equation (5). Note that $V_0$, a reference velocity in RSF, now influences stability. As the $\ln(V/V_0)$ term is directly multiplied by the parameter $a$, $V_0$ regulates the temporal influence of $a(V)$ on friction ($\mu$) and therefore influences the linear stability. In turn, this means that $V_0$ is not just a reference parameter, but must have a physical meaning. However, to define $V_0$ is beyond the scope of this work. Here we assumed $V_0=10^{-9}$ m s$^{-1}$, which results in a stability transition that roughly fits the laboratory observations for our velocity-dependent parameter case (Extended Data Fig. 2).

**Input parameters.** For simulations of laboratory experiments (Figs. 1 and 2), we used parameters determined in experiments[16] (on fine granular quartz): $a=0.005$, $b=0.01$, $D_c=10$ μm, $K=2$ GPa m$^{-1}$ and $M=200$ kg m$^{-2}$. Here $M=200$ kg m$^{-2}$ presents 4 kg of mass with 10 cm × 20 cm of contact area. Considering the quasi-static critical stiffness ($K_{c,qs}=(b-a)\sigma'/D_c$), our input parameters predicted a stability transition at a normal stress of 4 MPa, in agreement with experimental results at low loading rates. For the velocity-dependent RSF parameter case, we set $a_0=0.005$, $S_a=0.0003$ per decade, $V_a=100$ μm s$^{-1}$, $D_{c0}=10$ μm, $S_{D_c}=30$ μm per decade and $V_{D_c}=100$ μm s$^{-1}$. The cutoff velocity $V_a=V_{D_c}=100$ μm s$^{-1}$ was determined from quartz-gouge experiments[29] that used material similar to that for slow slip experiments[16] (Extended Data Fig. 3a). The velocity-dependent $a$ case and $D_c$ case shown in Fig. 2 also use identical parameters, except $S_a=0.0006$ per decade and $S_{D_c}=60$ μm per decade respectively.

For upscaled simulations (Fig. 3), we set parameters on the basis of laboratory data for material sampled from natural subduction faults, which are typically clay rich. These parameters included a constant $b=0.006$ and a depth-dependent $a_0$, which ranged from 0.009 to 0.003; $a_0$ increased linearly from 0 to 15 km, remained constant between 15 and 30 km and decreased linearly from 30 to ~45 km (Fig. 3b). Boundaries between velocity strengthening and weakening occurred at depths of 7.5 and 37.5 km, respectively. We set $V_a=V_{D_c}=0.5$ nm s$^{-1}$, $S_a=0.0013$ (Extended Data Fig. 3b) and $K=4$ MPa m$^{-1}$ (equivalent to a slip patch size of $L=10$ km).

**Slow slip data.** In the case of Cascadia (Fig. 4a), the slip model was derived from the inversion of geodetic time series[33]. We selected the time history of the slip on the northern segment of the Cascadia subduction zone, where the signal-to-noise ratio is best and nucleation occurs most frequently (at latitude ~48° N (ref. [33])). In the other examples, we selected representative time series at particular GPS stations. We rescaled each time series for slip on the megathrust on the basis of published fault slip inversions[6,33–35] (second $y$ axis in Fig. 4b–d), which assumes that repeated SSEs result from slip on the same segment and that GPS displacement varies linearly with fault slip. The long-term trend was subtracted from data.

**Simulation method.** We conducted simulations using a method that provides numerical stability in all slip modes—stable sliding, stick–slip and harmonic vibrations[41,46]. The velocity at each numerical step was constrained by the force balance. The time-discretized equation for displacement is:

$$\delta^{i+1} = \left[\delta^i - \left(\delta_{lp}^{i+1} - \mu^{i+1}\sigma/K\right)\right]\cos(\omega\Delta t) + \frac{V^i}{\omega}\sin(\omega\Delta t) + \left(\delta_{lp}^{i+1} - \mu^{i+1}\sigma/K\right) \quad (12)$$

where superscripts $i$ and $i+1$ denote successive time steps and $\omega$ is the angular frequency defined as $\omega=\sqrt{K/M}$ (see Im et al.[46] for details).

The numerical stability of the finite-difference scheme described by equation (12) requires $\Delta t \ll \omega$. This constraint is not troublesome if the total simulation time is sufficiently small. Hence, this method can be employed to simulate laboratory experiments (Figs. 1 and 2) due to the high loading rate ($V_l > 1\,\mu m\,s^{-1}$). However, the time-step constraint becomes a problem for upscaled simulations (Figs. 3 and 4) due to the long event recurrence ($t_r > 100\,yr$). In upscaled simulations, equation (12) is only adopted for the dynamic rupture phase. During static loading phases, equations (1), (2) and (3) are solved by simple discretization and coupling. A varied time step is implemented in the range 2 μs to 1 ms for laboratory parameter simulations and 100 ms to 10,000 s for upscaled simulations.

## Data availability

GPS data for Hikurangi and Ryuku are publicly available at the Nevada Geodetic Laboratory (http://geodesy.unr.edu/NGLStationPages/stations/GISB.sta and http://geodesy.unr.edu/NGLStationPages/stations/J750.sta). Mexico GPS data[35] and Cascadia inversion data[33] are available at the Caltech data repository[47] (https://doi.org/10.22002/D1.1286). Source data are provided with this paper.

## Code availability

Simulation codes are available at Caltech data repository[47] (https://doi.org/10.22002/D1.1286).

## References


38. Ruina, A. Slip instability and state variable friction laws. *J. Geophys. Res.* **88**, 10359–10370 (1983).
39. Ampuero, J. P. & Rubin, A. M. Earthquake nucleation on rate and state faults–aging and slip laws. *J. Geophys. Res.* **110**, 1–24 (2008).
40. Bhattacharya, P., Rubin, A. M., Bayart, E., Savage, H. M. & Marone, C. Critical evaluation of state evolution laws in rate and state friction: fitting large velocity steps in simulated fault gouge with time-, slip- and stress-dependent constitutive laws. *J. Geophys. Res. Solid Earth* **120** https://doi.org/10.1002/2015JB012437 (2015).
41. Im, K., Marone, C. & Elsworth, D. The transition from steady frictional sliding to inertia-dominated instability with rate and state friction. *J. Mech. Phys. Solids* https://doi.org/10.1016/j.jmps.2018.08.026 (2019).
42. Dieterich, J. H. Earthquake nucleation on faults with rate and state dependent strength. *Tectonophysics* **211**, 115–134 (1992).
43. Ikari, M. J., Marone, C., Saffer, D. M. & Kopf, A. J. Slip weakening as a mechanism for slow earthquakes. *Nat. Geosci.* **6**, 468–472 (2013).
44. Saffer, D. M. & Wallace, L. M. The frictional, hydrologic, metamorphic and thermal habitat of shallow slow earthquakes. *Nat. Geosci.* **8**, 594–600 (2015).
45. Ikari, M. J. & Kopf, A. J. Seismic potential of weak, near-surface faults revealed at plate tectonic slip rates. *Sci. Adv.* **3**, e1701269 (2017).
46. Im, K., Elsworth, D., Marone, C. & Leeman, J. The impact of frictional healing on stick–slip recurrence interval and stress drop: implications for earthquake scaling. *J. Geophys. Res. Solid Earth* **122**, 10102–10117 (2017).
47. Im, K. *Slip Rate-Dependent Friction as a Universal Mechanism for Slow Slip Events (Version 1.0) (Data Set)* (CaltechDATA, 2020); https://doi.org/10.22002/D1.1286
48. Okada, Y. Surface deformation due to shear and tensile faults in a half-space. *Bull. Seismol. Soc. Am.* **75**, 1135–1154 (1985).


## Acknowledgements

We thank to J. Leeman, S. Michel and A. Gualandi for sharing data. This study was supported by NSF EAR-1821853 to J.-P.A., NSF EAR-1616664 and OCE-1334436 to D.S. and NSF EAR-1763305 and EAR-1520760 to C.M.

## Author contributions

K.I. led the numerical modelling effort and writing of the manuscript. All the authors contributed to the interpretation of modelling results and writing the manuscript. D.S. and C.M. initiated the study and contributed to experimental data analysis. K.I. and J.-P.A. led the GPS data analysis.

## Competing interests

The authors declare no competing interests.

## Additional information

**Extended data** is available for this paper at https://doi.org/10.1038/s41561-020-0627-9.

**Supplementary information** is available for this paper at https://doi.org/10.1038/s41561-020-0627-9.

**Correspondence and requests for materials** should be addressed to K.I.

**Peer review information** Primary Handling Editor: Stefan Lachowycz.

**Reprints and permissions information** is available at www.nature.com/reprints.

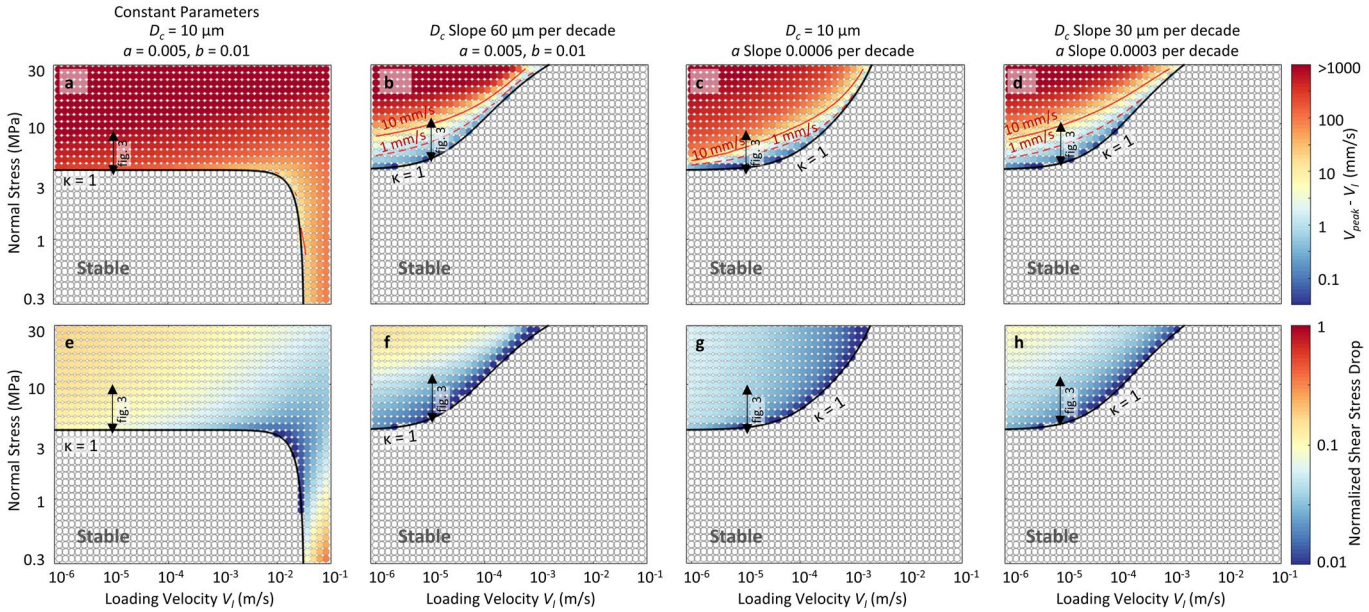


**Extended Data Fig. 1 | Evolution of peak velocity and stress drop with stability transition. a**, **e**, constant parameter, **b**, **f**, velocity dependent $D_c$, **c**, **g**, velocity dependent $a$, **d**, **h**, velocity dependent $D_c$ and $a$ cases. Panels a and d are identical to Figs. 1a and 1b, respectively. We used, $D_{c0} = 10\,\mu m$, $S_{Dc} = 60\,\mu m$ and $V_{Dc} = 100\,\mu m/s$ for velocity dependent $D_c$ and $a_0 = 0.005$, $S_a = 0.0003$, $V_o = 100\,\mu m/s$ for velocity dependent $a$ simulations.

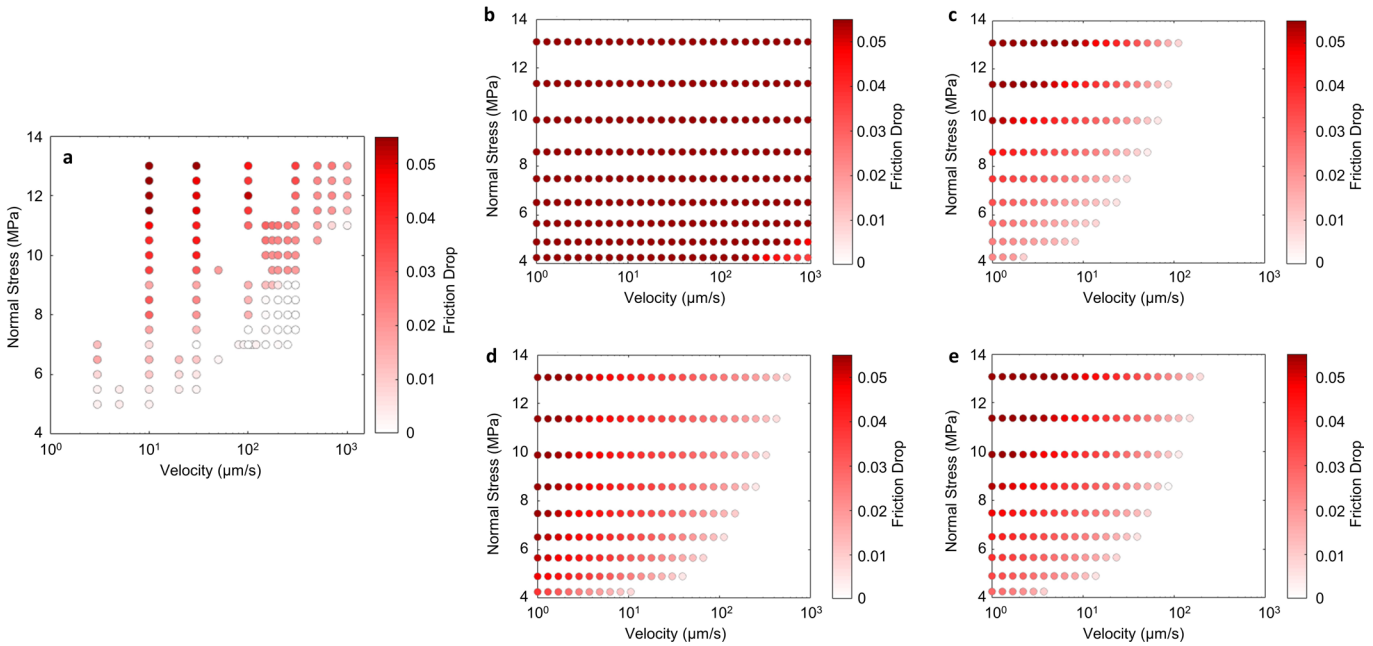


**Extended Data Fig. 2 | Comparison of stability transition between laboratory data and simulation results.** Friction drop as a function of normal stress and loading velocity for **a**, laboratory experiments[16], and **b-e**, simulations with **b**: constant parameters, **c**: velocity dependent $D_c$, **d**: velocity dependent $a$, and **e**: velocity dependence of both $a$ and $D_c$. Simulation results in **b-e** are identical to Extended Data Fig. 1e–h, but re-sized to match the laboratory results of Panel **a**.

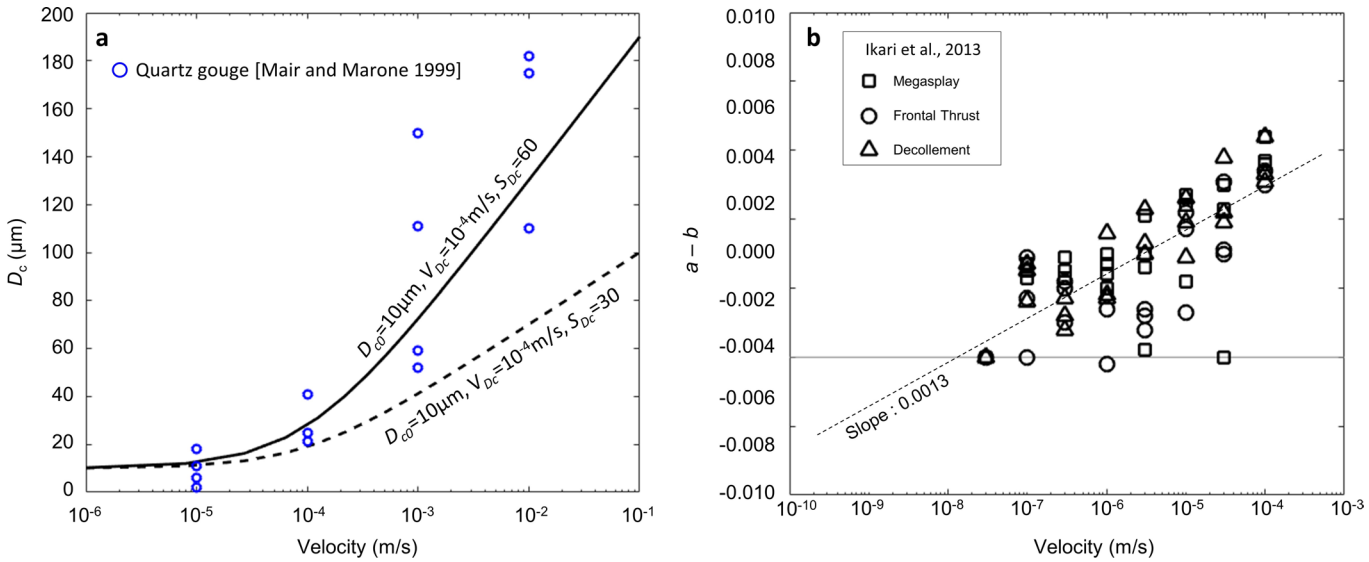


**Extended Data Fig. 3 | Experimental data for velocity dependence of friction parameters. a**, Experimental data showing $D_c$ as a function of sliding velocity for quartz gouge[29]. Blue circles are measurements and solid line represents the velocity dependence we used in our laboratory scale simulations (Figs. 1 and 2). For tectonic fault zone simulations, we used identical $S_{Dc}$, but with $D_{c0}=100\,\mu m$ and $V_{Dc}=10^{-9}$ m/s. **b**, Compiled experimental data for *a-b* on tectonic fault zone materials[27]. Dashed line denotes the trend line of all measurement. We used the slop of the trendline (0.0013 per decade) for upscaled (Fig. 3) simulations.

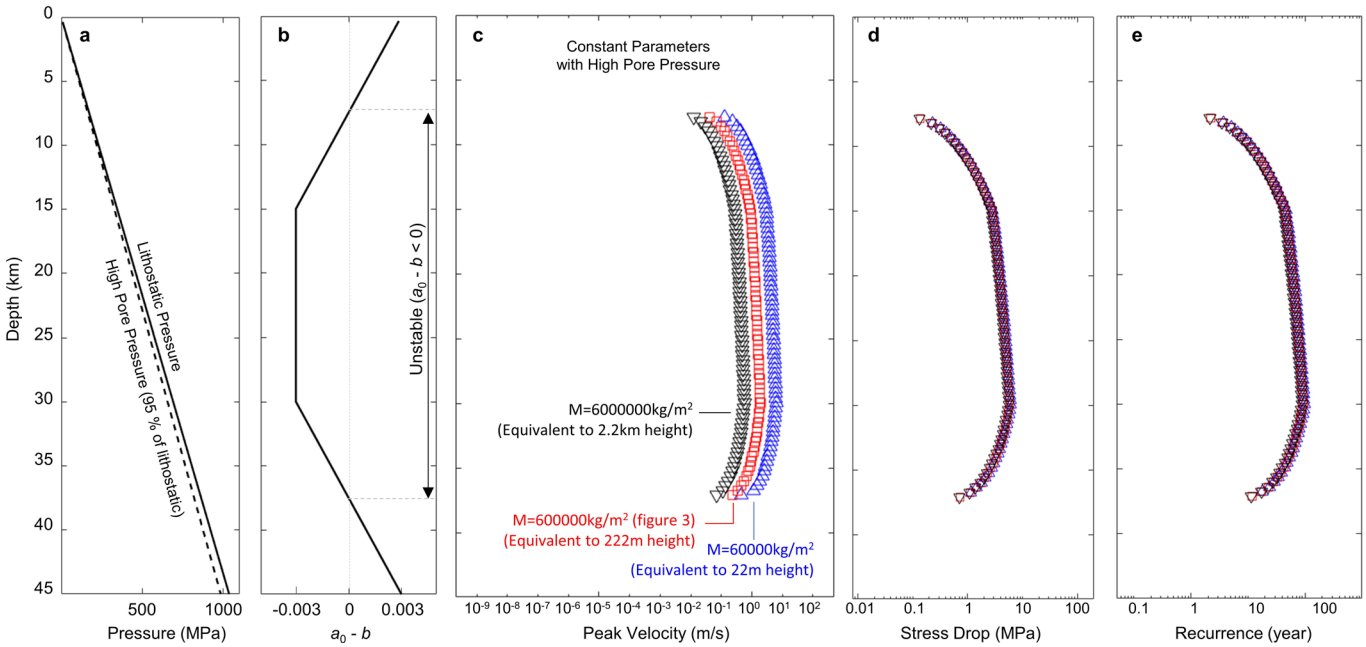


**Extended Data Fig. 4 | Influence of simulation mass on earthquake slip rate.** Here we only considered constant parameter RSF cases, with high pore pressure. Red squares (M = 600000 kg/m$^2$) are identical to main text Fig. 3 gray squares (Constant parameters high pore pressure). Blue and black squares show cases with one order of magnitude smaller and larger mass, respectively. Panel **c** shows that the peak velocity is dependent on the mass. However, even we assume significantly larger mass, stick slip abruptly evolves to fast rupture ($V_{peak}$ > 1 cm/s) at the transition.

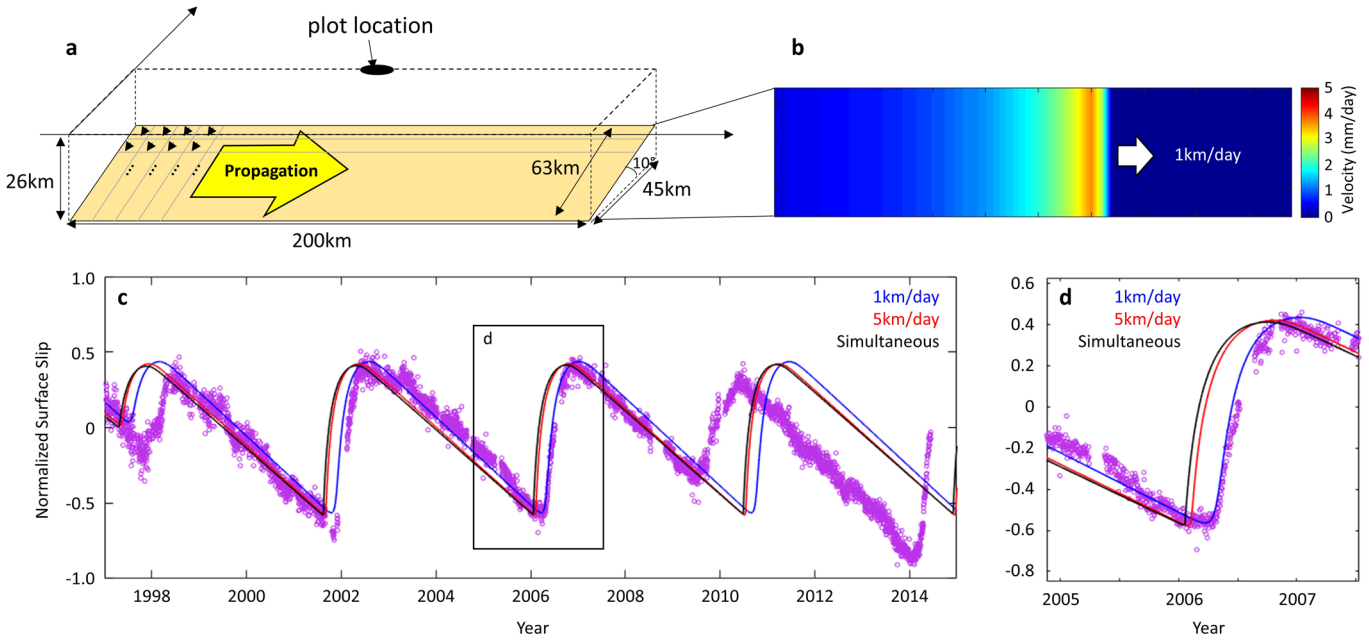


**Extended Data Fig. 5 | Simple kinematic model for slip propagation. a**, Model illustration. We assume 200 km × 63 km slipping patch (light yellow) embedded in a half space with its lower edge at a depth of 26 km. For displacement of each patch, we impose the time evolution of slip derived from the spring-slider model adjusted to the Guerrero example (Fig. 4d). We considered three cases for slip propagation along the strike direction at: (i) 1 km/day, (ii) 5 km/day, and (iii) a case with simultaneous slip in the entire patch. Panel **b**, shows an example of slip propagation for the 1 km/day case. The fault slip is converted to surface deformation using an elastic dislocation (Okada) model[48] and the normalized displacements are plotted in panels **c**&**d**, for comparison with the observed Guerrero gap GPS timeseries. The result shows that the case with a propagation rate of 5 km/day (red) is nearly indistinguishable from the case of simultaneous slip (equivalent to an infinitely fast propagation). The case with 1 km/day (blue) which is at the lower end of the typical rate of propagation of SSEs, is also only slightly altered by the effect of the propagation.